ACS OMEGA

http://pubs.acs.org/journal/acsodf

Article

Rational Design of Hierarchical Structural CoSe@NPC/CoSe@CNT Nanocomposites Derived from Metal–Organic Frameworks as a Robust Pt-free Electrocatalyst for Dye-Sensitized Solar Cells

Tong Wang,[§] Yongjian Li,[§] Hansheng Li,* Daxin Shi, Qingze Jiao, Yun Zhao, Pengju Su, Wei Wang, and Qin Wu*

Cite This: *ACS Omega* 2020, 5, 26253–26261

Read Online

ACCESS | Metrics & More | Article Recommendations | Supporting Information

ABSTRACT: Transition-metal compounds/carbon hybrids with high electrocatalytic capability possess attractive potential as a counter electrode (CE) for dye-sensitized solar cells (DSSCs). However, the simple structure and agglomeration always result in poor performance. Herein, cobalt selenides confined in hollow N-doped porous carbon interconnected by carbon nanotubes (CNTs) with cobalt selenides encapsulated inside (denoted as CoSe@NPC/CoSe@CNTs) are formed through *in situ* pyrolysis and selenization process. In this strategy, ZIF-67 is used as the precursor, structure inducer, and carbon source for the orientated growth of CNTs. Such a rational architecture provides a stable interconnected conductive network and a hierarchically porous structure, with more available active sites and a shortened pathway for charge transport, synergistically enhancing the electrocatalytic activity. Specifically, the DSSCs based on CoSe@NPC/CoSe@CNTs demonstrate a high efficiency of 7.36%, even superior to that of Pt (7.16%). Furthermore, the CoSe@NPC/CoSe@CNT CE also demonstrates a good long-term stability in the iodine-based electrolyte.

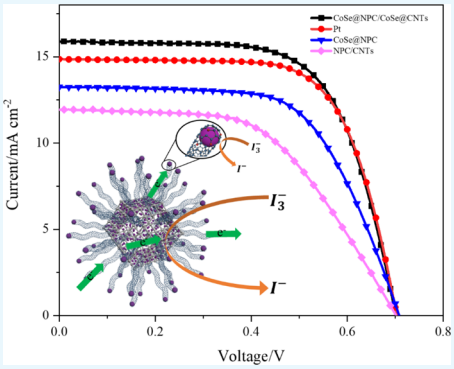

1. INTRODUCTION

The rational use of solar energy resources is of great significance to address the issues of energy shortage and greenhouse effect. Dye-sensitized solar cells (DSSCs) have sparked extensive attention around the world since Grätzel sharply increased the power conversion efficiency (PCE), primarily owing to its easy manufacturing process, low cost, and environmental friendliness.[1,2] The counter electrode (CE), as an important component of a standard DSSC device, is responsible for collecting electrons from the outer circuit and catalyzing the conversion of triiodide to iodide in an organic solvent.[3−5] At present, a platinum-plated conductive glass is regarded as the state-of-the-art CE for DSSCs in virtue of high conductivity and excellent electrocatalytic ability of noble metal Pt.[6] Nevertheless, the relatively expensive price and scarcity of resources of Pt, as well as its poor long-term duration in redox electrolytes (I_3^-/I^-), have become one of the main bottlenecks for large-scale commercial application of DSSCs.[7−9] Hence, a continuous scientific endeavor has been devoted to developing effective and inexpensive Pt-alternative materials in recent decades.[8−12]

Among the studied precious metal-free alternatives, transition-metal compounds/nitrogen-doped carbon materials have proven their great promise as electrocatalysts for iodide reduction reaction (IRR).[13−18] Very recently, the zeolitic imidazolate framework-67 (denoted as ZIF-67), made up of cobalt ions as the coordination center and nitrogen-rich 2-metholinidazolate as the bridging organic ligand, has been extensively developed as a novel self-sacrificed template/precursor for fabricating transition-metal compounds/nitrogen-doped carbon nanostructures.[19,20] These ZIF-derived materials generally show exceptionally large pore volumes, tunability of structures, and adjustable pore sizes, which are particularly beneficial for charge and mass transfer during their electrocatalytic processes.[21,22] However, these materials are mostly subjected to several disadvantages, such as simple structures, inefficient electron transfer, and unexposed deeply buried catalytic active sites owing to spontaneous agglomeration of cobalt-based compounds during pyrolysis, which severely impeded their further applications.[23,24] Previous studies demonstrated that the surface morphology and microstructure play vital roles in improving electrical conductivity, electrocatalytic activity, and stability.[25−27] Therefore, the rational synthesis of multilevel structures from ZIFs

Received: August 19, 2020
Accepted: September 22, 2020
Published: October 2, 2020

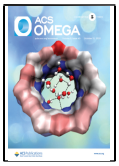

https://dx.doi.org/10.1021/acsomega.0c04022
ACS Omega 2020, 5, 26253−26261

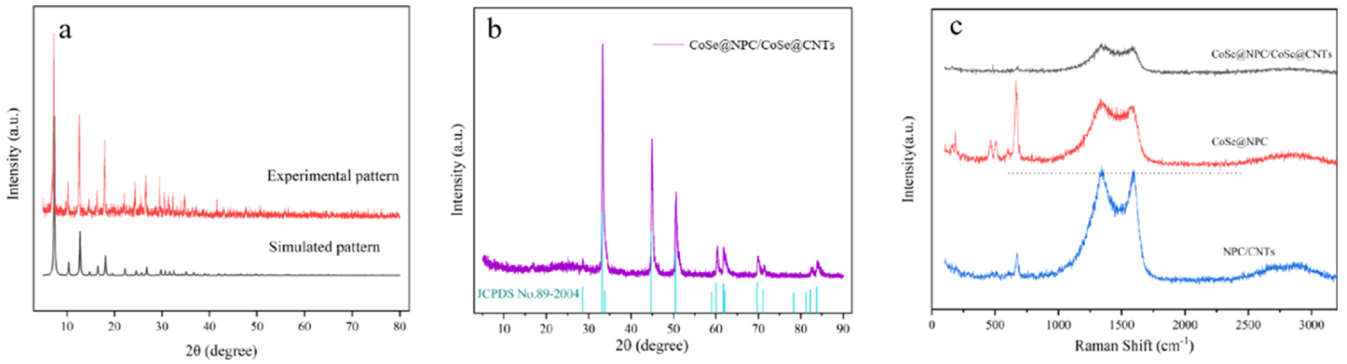

Figure 1. (a) XRD patterns of the as-obtained pure ZIF-67 and its theoretically simulated pattern, (b) XRD patterns of CoSe@NPC/CoSe@CNTs and the standard card of CoSe, and (c) Raman spectra of CoSe@NPC/CoSe@CNTs, CoSe@NPC, and NPC/CNTs.

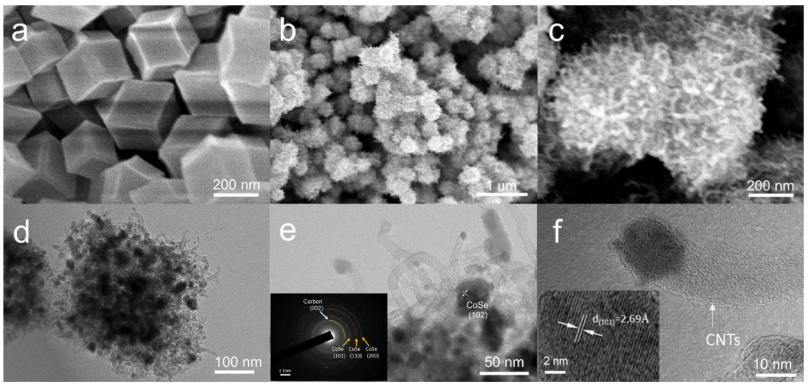

Figure 2. (a) SEM image of ZIF-67 polyhedrons, (b,c) SEM images, (d) TEM image, and (e,f) HRTEM images (the inset shows the corresponding SAED pattern and the diffraction fringe pattern individually) of CoSe@NPC/CoSe@CNTs.

by a general and efficient strategy is required to make a breakthrough.

Herein, we selected ZIF-67 as the precursor as well as the carbon source to construct a hollow hierarchical structure of CoSe@NPC/CoSe@CNTs by a one-step method. In this composite, hollow CoSe@NPC polyhedra possessed a hierarchical porous structure and an interior void, contributing to fast mass transport and utilization efficiency of active sites. In addition, CoSe@NPC was interconnected to form a stable conductive network by the *in situ* formed carbon nanotubes (CNTs), at the end point of which zero-dimensional CoSe nanoparticles were encapsulated in graphitic layers to form a synapse-like core−shell structure, which could maximize the effective exposure of catalytic sites, and ensure the structural durability. The synergistic effects of the above factors in CoSe@NPC/CoSe@CNTs ensure its excellent electrocatalytic properties toward triiodide reduction. When applied in DSSCs, CoSe@NPC/CoSe@CNTs could outperform the noble Pt with an efficiency of 7.36% and deliver a good long-term stability in the I_3^-/I^- electrolyte.

2. RESULTS AND DISCUSSION

X-ray diffraction (XRD) measurements were implemented to identify the phase composition and crystalline nature of as-prepared samples. As shown in Figure 1a, the powder XRD pattern of purple product matched well with the simulated of ZIF-67, especially in the range of 5−40°, indicating its good phase purity and crystallinity.[28] Moreover, the sharp diffraction peaks shown in Figure 1b were in agreement with the characteristic peaks of hexagonal freboldite CoSe (JCPDS no. 89-2004), and no other peaks were detected except the peak of graphite, demonstrating a complete phase transformation reaction to CoSe during the process of selenization.[29,30] The peak intensity was relatively large, implying its significant crystallinity. In addition, there was a broad diffraction peak near 26°, corresponded to the (002) plane of graphitic carbon, which was formed by carbonization of organic skeleton during the high-temperature pyrolysis.

Raman spectra were then obtained to characterize the degree of disorder and graphitization in carbonaceous materials by the intensity ratio of D and G bands (I_D/I_G). As shown in Figure 1c, the as-prepared three samples, CoSe@NPC/CoSe@CNTs, CoSe@NPC, and NPC/CNTs, displayed two distinct broader peaks at around 1335 and 1590 cm^{-1}, which was deemed to describe the disordered graphitic carbon (D band) and sp^2-bonded carbon (G band), respectively. Compared with CoSe@NPC (I_D/I_G = 1.08), there was a slight decrease in the disorder degree of CoSe@NPC/CoSe@CNTs (I_D/I_G = 1.06). It was shown that the graphitization degree of *in situ* formed CNTs was higher than that of NPC, which might be on account of the higher well-organized arrangement of carbon atoms in CNTs.[31,32] Further compared with NPC/CNTs (I_D/I_G = 1.02), the introduction of CoSe in CoSe@NPC/CoSe@CNTs increased the value of I_D/I_G, which might be the presence of more non-sp^2-bonded domain resulting from the defects near the interface between CoSe particles and the coated carbon layer. Other peaks at 666, 506, 460, and 184 cm^{-1}, presented in both spectra, were assigned to the crystalline structure of cobalt selenide.[33]

https://dx.doi.org/10.1021/acsomega.0c04022
ACS Omega 2020, 5, 26253−26261

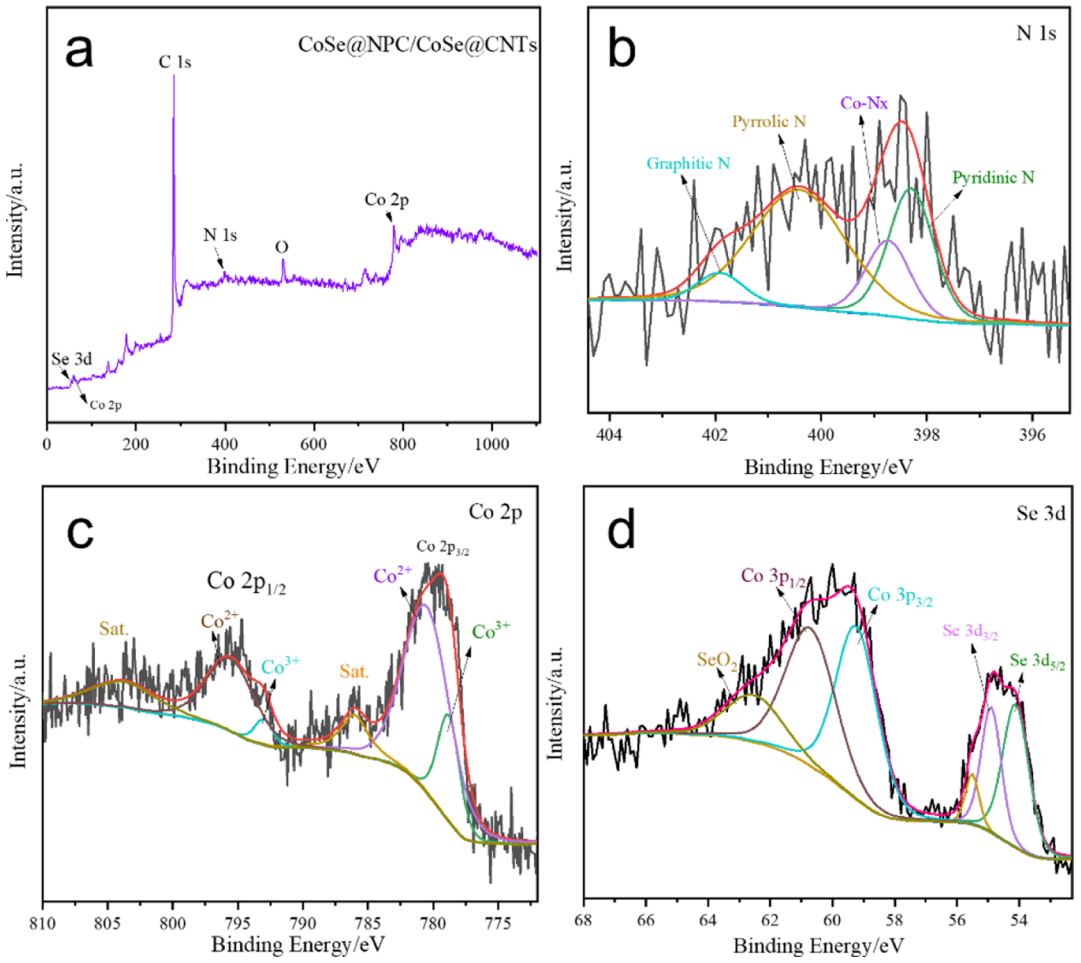

Figure 3. (a) XPS survey spectra and high-resolution XPS survey spectra of (b) N 1s and (c) Co 2p and (d) Se 3d of CoSe@NPC/CoSe@CNTs.

The morphology and microstructure of the as-prepared samples were characterized by field-emission scanning electron microscopy (FESEM) and transmission electron microscopy (TEM). As displayed in Figure 2a, the prism crystal ZIF-67 exhibited a smooth surface and monodispersed particle distribution with an average size of 300 nm, in agreement with previous reports.[34] After thermal treatment, ZIF-67 was transformed into CoSe@NPC/CoSe@CNTs with the general oriented growth of a broad set of CNTs on the primary plane, and the size and polyhedral shape were well preserved, as confirmed by Figure 2b. Meanwhile, Figure 2c demonstrates the spatial interconnected conductive network, where the cross-linked CNTs bridged the adjacent ZIF-67-derived particles. Thus, it prevented the individual particle from agglomeration. The TEM images (Figure 2d) further show that the average particle size of CoSe@NPC was about 500 nm (Figure 2a,b), and CoSe nanoparticles were embedded in the hollow N-doped porous carbon skeleton. These thin CNTs could also be observed in Figure 2e, with outer diameters ranging from 10 to 20 nm and lengths ranging from 100 to 150 nm. Interestingly, the ultrafine CoSe nanocrystals of *ca.* 15 nm were encapsulated firmly in graphitic layers within the apexes of CNT, which was similar to the synapse structure and could adequately expose the catalytic active sites to the electrolyte.

Typical high-resolution TEM (HRTEM) (Figure 2f) images provided direct evidence that the multiwalled CNTs were crystalline and composed of graphitic carbon layers with a clear interlayer spacing of 0.34 nm, corresponded to the C (002) lattice plane. Figure 2f also reveals a clear lattice distance of 0.269 nm corresponded to the (101) lattice plane of CoSe, which was in line with the XRD result. It was noteworthy that the graphitic carbon layers in the walls were not perfectly parallel to the axial direction of the CNTs because of nitrogen doping, suggesting more defects and edges in the CNTs, which would be conducive to the enhanced electrocatalytic property.[35] The selected area electron diffraction (SAED) pattern inset in Figure 2e also exhibits different rings assigned to the (101), (110), and (102) diffraction of CoSe and the (002) diffraction of carbon.[36] Moreover, thermogravimetric analysis (TGA) was carried out in air atmosphere to estimate the CoSe contents in the sample of CoSe@NPC/CoSe@CNTs. According to the calculation method reported previously,[37] the CoSe contents in the sample of CoSe@NPC/CoSe@CNTs is 71%.

X-ray photoelectron spectroscopy (XPS) was carried out to analyze the near-surface elemental compositions and chemical states of CoSe@NPC/CoSe@CNTs. The XPS survey spectrum shown in Figure 3a indicated the presence of Co, O, N, C, and Se elements, in which the appearance of oxygen might be due to the exposure and unavoidable surface adsorption in the air atmosphere.[38] The regional C 1s spectrum in Figure S3 was deconvoluted into three different peaks located at 284.5, 285.3, and 288.9 eV, which were corresponded to the C═O, C−C−O, and sp^2-bonded C−C−C functional groups, respectively. The N 1s spectrum (Figure 3b) could be deconvoluted into graphitic N located at 401.9

https://dx.doi.org/10.1021/acsomega.0c04022
ACS Omega 2020, 5, 26253−26261

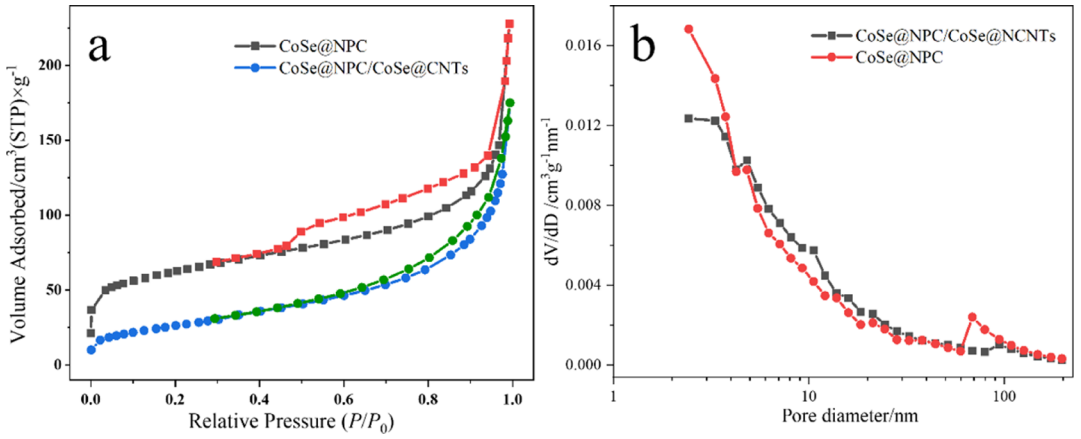

Figure 4. (a) N_2 adsorption−desorption isotherms and (b) pore size distribution curve of CoSe@NPC/CoSe@CNTs and CoSe@NPC.

eV, pyrrolic N at 400.4 eV, Co-coordinated N (Co-Nx) at 398.7 eV, and pyridinic N at 398.3 eV, respectively. The N-doping can not only directly bond with carbon and metal atoms but also enrich the conjugated electrons and facilitate the electronic conductivity, enabling enhancement in the electrochemical performance.[39] Of particular note, among the four types of N, the pyridinic N and Co-Nx were recognized as the highly active sites, which generally played a key role in IRR electrocatalytic activity.[40−42] Interestingly, the content of these two types of N was 42.8%, which made CoSe@NPC/CoSe@CNT composites excellent for catalyzing the reduction of triiodide. The high-resolution spectrum of Co 2p (as presented in Figure 3c) exhibited two distinct spin−orbit doublets, which was further deconvoluted into Co^{2+} oxidation state located at the binding energies of 790.8 and 795.9 eV and Co^{3+} oxidation state at 778.9 and 793.1 eV.[43] The two binding energies located at 54.1 and 54.9 eV of the Se 3d spectrum (Figure 3d) corresponded to Se $3d_{5/2}$ and Se $3d_{3/2}$, respectively. The peaks in the range of 58−64 eV were assigned to the Co 3p energy level and Se−O bonding at the surface of composites owing to the partial surface exposure in air.[44]

The surface area and pore size distribution of CoSe@NPC/CoSe@CNTs and CoSe@NPC were then identified by the N_2 absorption−desorption isotherm at 77 K. As shown in Figure 4a, these two N_2 adsorption and desorption isotherms displayed typical IV isotherms with type H3 hysteresis loops, implying the presence of mesoporous structures.[45] Notably, compared with the Brunauer−Emmett−Teller (BET) surface areas of CoSe@NPC (219.56 $m^2\ g^{-1}$), a distinct reduction of that of CoSe@NPC/CoSe@CNTs (95.28 $m^2\ g^{-1}$) was found, owing to the consumption of carbon sources by *in situ* formed CNTs at the high temperature, which influenced the growth of porous structure of NPC. Meanwhile, the results also implied the abundant pores of NPC compared with CNTs. The pores of CoSe@NPC/CoSe@CNTs, fitted by the Barrett−Joyner−Halenda (BJH) method and based on the desorption branch, were mainly distributed around the size of 2−30 nm, showing a hierarchical porosity. In addition, the number of pores around 70−80 nm of CoSe@NPC were more than that of CoSe@NPC/CoSe@CNTs, which might be a part of CoSe nanoparticles wrapped by CNTs, rather than inset onto NPC, giving rise to the decrease of carbon pores of NPC of CoSe@NPC/CoSe@CNTs. Such a hierarchically porous structure and suitable pore size distribution could accelerate the charge transfer at the electrode/electrolyte interface and shorten the diffusion pathways for electrolytes.

To investigate the formation mechanism of CoSe@NPC/CoSe@CNTs, the ZIF-67 precursor were put into the furnace to undergo the same heating program under argon without Se powder and H_2, respectively. Figure S4a,b displays the XRD pattern and SEM images of the intermediates. According to the XRD pattern, metallic Co was obtained without the Se powder. The SEM images illustrated that Co@CNT components had been constructed before selenization, while CoSe@NPC could be obtained without H_2 as shown in Figure S5a−c. The CoSe nanoparticles were also uniformly encapsulated in NPC. On the basis of these observations, the possible formation mechanism was discussed as follows and is schematically provided in Scheme 1. During the pyrolysis process, the

Scheme 1. Schematic Illustration for the Formation of CoSe@NPC/CoSe@CNTs

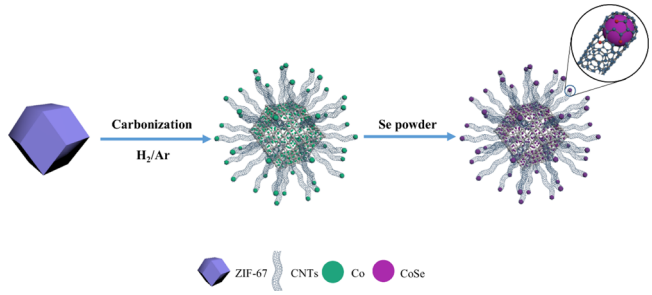

coordination bonds between metal ions and organic ligands in the ZIF-67 break first, and then the Co ions were reduced to metallic Co clusters/nanoparticles by the reducing gases. In addition, the organic ligands suffered degeneration and carbonization to form the N-doped porous carbon matrices, and then carbon atoms were further catalyzed into CNTs by the metallic Co. Because of the preferential catalysis of metallic Co with proper size on the surface, the ultrafine CNTs grew from inside to outside, leading to hollow interior voids. As the reaction progressed, the metallic Co reacted with Se source and integrated to form the highly crystalline freboldite CoSe nanoparticles. In the whole process, the ZIF-67 dodecahedra as a single precursor and carbon sources oriented the *in situ* growth of CNTs and were eventually converted into morphology-preserved CoSe@NPC/CoSe@CNTs.

https://dx.doi.org/10.1021/acsomega.0c04022
ACS Omega 2020, 5, 26253−26261

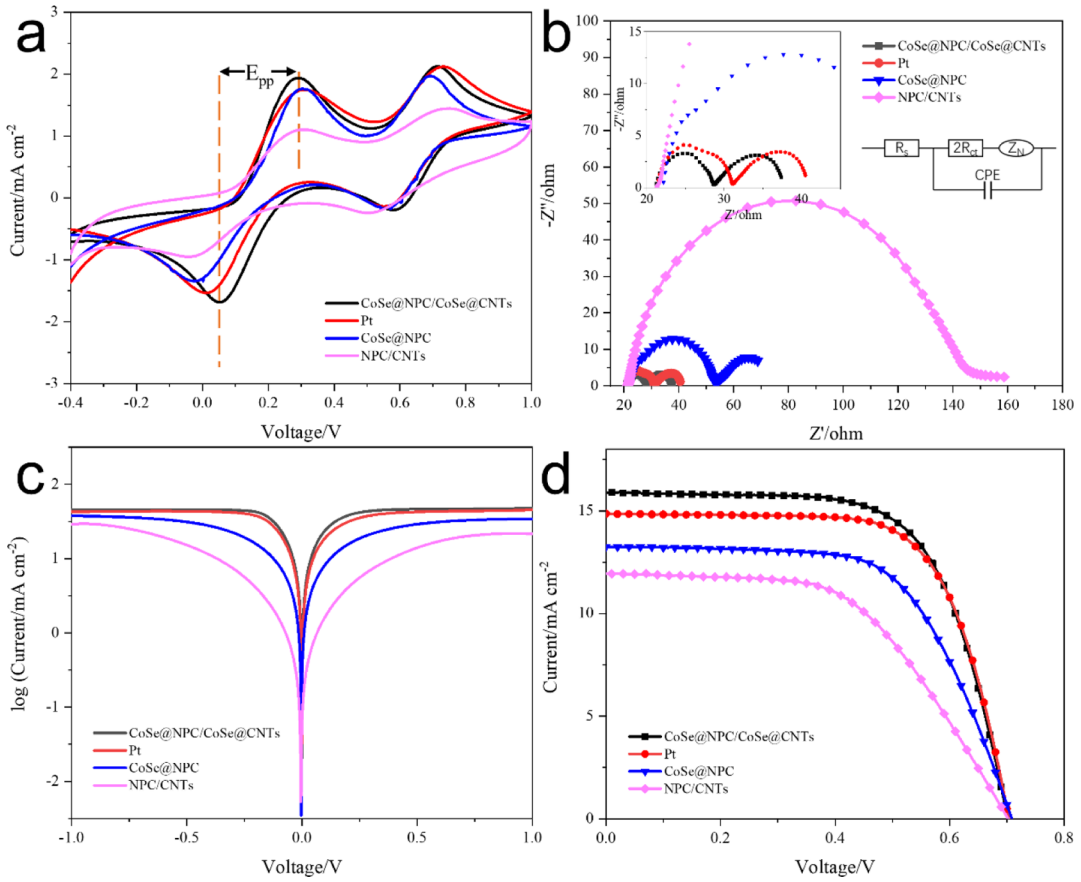

Figure 5. (a) CV curves, (b) Nyquist plots, and (c) Tafel polarization curves of CoSe@NPC/CoSe@CNTs, Pt, CoSe@NPC, and NPC/CNTs samples and (d) *J*−*V* curves of DSSCs with the above different CEs.

Table 1. Detailed Photovoltaic Parameters and EIS Parameters of As-Prepared CEs

	R_s (Ω)	R_{ct} (Ω)	Z_N (Ω)	V_{oc} (V)	J_{sc} (mA cm^{-2})	FF	PCE (%)
CoSe@NPC/CoSe@CNTs	20.60	3.56	4.16	0.701	15.90	0.66	7.39
Pt	20.89	4.94	3.61	0.704	14.86	0.68	7.16
CoSe@NPC	22.67	14.90	12.52	0.709	13.25	0.63	5.89
NPC/CNTs	21.73	64.25	41.29	0.702	11.93	0.54	4.54

On account of energy conservation and facial synthesis in the preparation process, controllable morphology, and degree of crystallinity of the final products, we have designed two independent heating programs in a multisection temperature-programmed furnace (MSTPE) as delineated below: section I, part of the quartz tube inside which precursor ZIF-67 stored in a quartz boat was placed, heated from room temperature to 570 °C with a ramp rate of 10 °C min^{-1}, and maintained for 180 min for use in the adequate carbonization of ZIF-67. The selenization and crystallization temperature of the sample prepared by carbonization of ZIF-67 in section I can influence the crystal structure, obtain a thermodynamically stable crystal phase, and increase the conductivity of the as-synthesized samples. When 600 °C, rather than 650 °C, was chosen as the final plateau temperature of section I, the XRD pattern of the as-prepared sample (shown in Figure S6) indicated the existence of hexagonal CoSe (JCPDS no. 89-2004), as well as orthorhombic $CoSe_2$ (JCPDS no. 53-0449) and cubic Co (JCPDS 88-2325). (The corresponding heating program is displayed in Figure S2.) Accordingly, 650 °C was suitable to gain the phase of CoSe with high crystallinity during the process of selenization and crystallization. In the end, section I was heated with a heating rate of 10 °C min^{-1} from 570 to 650 °C and maintained for 180 min. Meanwhile, section II, another part of the quartz tube and placed with Se powder, was heated from room temperature to 300 °C at a low heating rate of 2 °C min^{-1} and maintained for 53 min to prevent the evaporation loss of Se powder as at the same time the ZIF-67 in section I was under high-temperature carbonization. Universally, the evaporation rate of Se sources is vital for the complete chemical transformation of metallic cobalt to CoSe. For controlling the gasification rate of Se powder, the following rate of 10 °C min^{-1} from 300 to 400 °C and the holding time of 60 min were then adopted. (The heating program of MSTPE is displayed in Figure S1.)

In this work, electrochemical impedance spectroscopy (EIS) was first performed to analyze the details about the interfacial charge-transfer process. Figure 5b displays the Nyquist plots obtained by using symmetrical sandwich-type cells composed of two identical CEs, and the relevant impedance parameters obtained by fitting the Nyquist plots with the Z-view software are listed in Table 1. As illustrated in the equivalent circuit diagram inserted in Figure 5b, the left high-frequency intercept on the real axis is series resistance (R_s), associated with the

https://dx.doi.org/10.1021/acsomega.0c04022
ACS Omega 2020, 5, 26253−26261

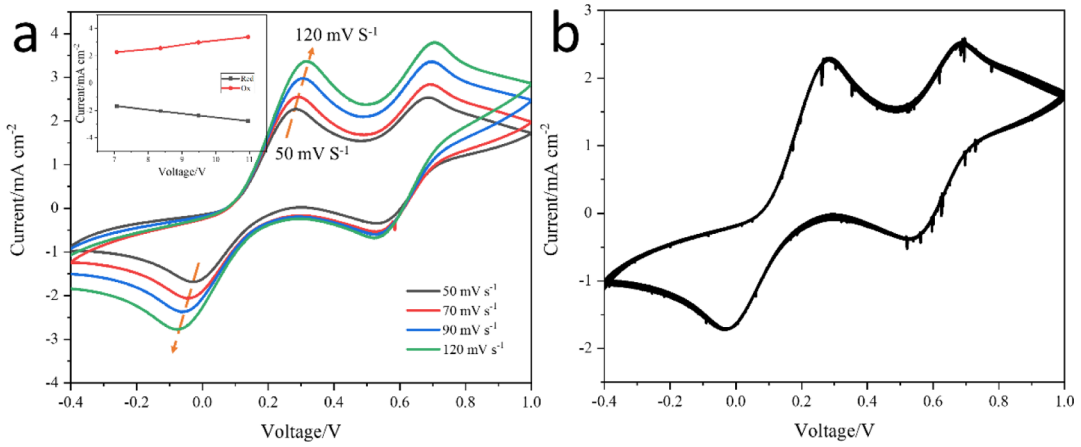

Figure 6. (a) CV curves of CoSe@NPC/CoSe@CNT CE at different scan rates (from inner to outer: 50, 70, 90, and 120 mV s^{-1}, respectively) and (b) CV curves of CoSe@NPC/CoSe@CNT CE obtained for successive 50 cycles at a scan rate of 50 mV s^{-1}. The inset in (a) illustrated the relationship between the redox peak currents and the square root of the scan rate.

electrical conductivity of CEs. The order of R_s values was NPC/CNTs < CoSe@NPC/CoSe@CNTs < Pt < CoSe@NPC, which were attributed to the low electric resistance and better ohmic contact of interconnected NPC/CNTs. The left high-frequency semicircle represents charger-transfer resistance (R_{ct}), reversely related to electrocatalytic activity, while the right one at the low-frequency region represents Nernst diffusion impedance (Z_N), stemming from the mass transport limitation due to the diffusion of the I_3^-/I^- redox shuttle. Apparently, the R_{ct} values increased in the order of CoSe@NPC/CoSe@CNTs (3.56 Ω) < Pt (4.94 Ω) < CoSe@NPC (14.90 Ω) < NPC/CNTs (64.25 Ω). The superior intrinsic catalytic activity of CoSe could be testified by the fact that the CoSe@NPC CE showed a much smaller R_{ct} in comparison to that of NPC/CNTs. It was thus concluded that the CoSe@NPC/CoSe@CNT CE had a remarkable electrocatalytic ability for I_3^- reduction. Such a quite low R_{ct} was attributed to the unique structural advantage of NPC/CNT-encapsulated CoSe nanoparticles, hence facilitating electron transfer from carbon skeletons directionality to the highly active metal centers. Moreover, the Z_N of CoSe@NPC/CoSe@CNT CE (4.16 Ω) was also lower than that of the others, revealing a higher diffusion coefficient of the porous carbon skeletons for I_3^-.

Tafel polarization curve measurements were then carried out on the same symmetric cells used in EIS experiments, and the corresponding plots are shown in Figure 5c. The limiting diffusion current density (J_{lim}) and the exchange current density (J_0) obtained from Tafel curves have a positive correlation with the electrocatalytic activity of CEs and the diffusion characteristics of redox couple, respectively. The relationship between the conclusions of the EIS and Tafel results can be demonstrated by eq $J_0 = RT/nFR_{ct}$, where R is the gas constant, T is the absolute temperature (298 K), n is the number of electrons involved in the triiodide reduction, and F is Faraday's constant.[46] As Figure 5c depicts, the values of J_0 decreased in the order of CoSe@NPC/CoSe@CNTs > Pt > CoSe@NPC > NPC/CNTs. Similarly, the J_{lim} values were also in the decreasing sequence of CoSe@NPC/CoSe@CNTs > Pt > CoSe@NPC > NPC/CNTs. The trend of J_0 and J_{lim} matched well with the results of EIS experiments and further demonstrated the highest catalytic activity and exceptional diffusion property for triiodide reduction of hierarchical structural CoSe@NPC/CoSe@CNT CE.

Cyclic voltammetry (CV) measurements were conducted to further elucidate the catalytic activity and electrochemical behavior of as-prepared CEs. As presented in Figure 5a, two distinct pairs of oxidation/reduction peaks were unambiguously observed for all electrodes, with the left pair for the redox reaction of $I_3^- + 2e^- \rightarrow 3I^-$ (Red-1/Ox-1) and the right one for the redox reaction of $3I_2 + 2e^- \rightarrow 2I_3^-$ (Red-2/Ox-2). In DSSCs, the cathodic peak current density of Red-1 and the peak-to-peak separation (E_{pp}) between Red-1 and Ox-1 are two crucial parameters, which are interrelated to the reduction velocity and the reversibility of the redox reaction, respectively. The CoSe@NPC/CoSe@CNT CE delivered the highest $J_{Red\text{-}1}$ and smallest E_{pp}, even superior to that of Pt, which confirmed the faster reaction kinetics in catalyzing the triiodide reduction, consistent with the results of EIS analysis. The better electrocatalytic activity arouse from the appropriate N doping and confined CoSe nanoparticles in NPC/CNTs, which could increase the densities of states near the Fermi level and reduce the work function.[32]

The ---photocurrent density−voltage (J−V) curves of the DSSCs based on different CEs were obtained under the standard AM 1.5 irradiation (100 mW cm^{-2}), and their detailed parameters are also recorded in Table 1. As for the NPC/CNT CE treated with acid, a decrease in performance was observed, with the corresponding values of V_{oc} (0.702 V), J_{sc} (11.93 mA cm^{-2}), FF (0.54), and a lower conversion efficiency (4.54%), which further demonstrated that CoSe was the main active constituent. It is noteworthy that the DSSCs based on CoSe@NPC/CoSe@CNT CE possessed the best photovoltaic performance with a J_{sc} of 15.9 mA cm^{-2}, V_{oc} of 0.701, and FF of 0.66 and then gave the highest photovoltaic conversion efficiency of 7.39%, outperforming that of Pt (7.16%). The improved efficiency could be attributed to synergistic effects between ideal components and their hierarchical structure. The abundant pore structures and interior hollow voids of CoSe@NPC acted as an electrolyte reservoir promoting mass transport and accessibility of electrochemical active sites, while the *in situ* growth of CNTs onto the CoSe@NPC provided sufficient electron-transfer paths. More importantly, the CoSe nanoparticles encapsulated at the end point of CNTs, as well as the one

https://dx.doi.org/10.1021/acsomega.0c04022
ACS Omega 2020, 5, 26253−26261

confined onto the NPC skeleton, jointly contributed to the increased exposure of active centers, thus achieving a more efficient catalytic reduction process.

The stability of CoSe@NPC/CoSe@CNT CE was also tested by CV measurement. Figure 6a shows the CV curves of CoSe@NPC/CoSe@CNT CE at different scan rates. It could be found that the redox peak current densities gradually increased with the increase of scan rate from 50 to 120 mV s^{-1}. Moreover, a good linear relationship between the peak current density and the square root of the scan rate is observed in Figure 6a. It could thus be deduced that the redox reduction on the surface of CoSe@NPC/CoSe@CNT CE was dominated by the ionic diffusion in the electrolyte, and the redox couple had no specific effect on CoSe@NPC/CoSe@CNT CE. The consecutive CV measurement at a scan rate of 50 mV s^{-1} was also presented for CoSe@NPC/CoSe@CNT CE, as shown in Figure 6b. No obvious decline for peak current densities or peak shifts was observed after 50 cycles of scan, which indicated the excellent electrochemical stability in the I_3^-/I^- electrolyte. These negligible changes of redox peaks also implied that the CoSe@NPC/CoSe@CNT electrode film had tight adhesion on a fluorine-doped tin oxide (FTO)-conductive glass substrate. The outstanding electrochemical stability along with exceptional photoelectric conversion efficiency demonstrated that CoSe@NPC/CoSe@CNTs was a reliable CE material to replace noble Pt in DSSCs.

3. CONCLUSIONS

In summary, we reported a facile and energy-conserving strategy for the direct formation of CoSe@NPC/CoSe@CNTs by *in situ* pyrolysis−selenization of ZIF-67. This unique architecture possessed a plenty of advantages, including highly conductive networks, a N-doping porous carbon skeleton, abundant hierarchical porous structure, and more available active sites. Benefitting from the synergistic effect, the CoSe@NPC/CoSe@CNT composites demonstrated excellent electrocatalytic performance in DSSCs, with a high efficiency of 7.36%, outperforming the noble Pt. It can be expected that such an energy-efficient route could be extended to evaluate the electrochemical properties by designing and optimizing the hierarchical structure of ZIF-derived materials and obtain potential CE materials for high-performance DSSCs.

4. EXPERIMENTAL SECTION

4.1. Materials. All chemical reagents and solvents employed were purchased commercially and used as received without further purification. The substrates of N719 dye (*cis*-di(isothiocyanato)-bis-(2,20-bipyridyl-4,40-dicarboxylato) ruthenium(II) bis-tetrabutyl ammonium) and TiO_2 pastes (NJU-SR and NJU-SCL) were purchased from Dyesol (Australia) and Kunshan Sunlaite New Energy Co., Ltd (Nanjing, China), respectively.

4.2. Synthesis of ZIF-67 Nanocrystals. ZIF-67 nanocrystals were prepared based on a previously reported method with some modifications.[47]

Cobalt nitrate hexahydrate (1.445 g, $Co(NO_3)_2{\cdot}6H_2O$, 5 mmol) and 1.642 g of 2-methylimidazole (2-mIm, 20 mmol) were dissolved in 100 mL of methanol. Then, a 2-mIm solution was quickly poured into the former cobalt salt solution under vigorous stirring for 30 min at room temperature. After that, the resulting purple mixture was added inside an oven of a constant temperature of 25 °C to fully crystallize for 4 h. Finally, ZIF-67 was collected by centrifugation, washed with methanol several times, and dried in vacuum at 60 °C overnight.

4.3. Synthesis of Hierarchical Structural CoSe@NPC/CoSe@CNT Nanocomposites. The prepared 100 mg ZIF-67 and an appropriate amount of Se powder were placed in two individual quartz boats in a flow-through tube furnace. Then, the two boats were inserted into an MSTPE in which the porcelain containing Se powder was placed at the upstream side of the furnace. A reducing atmosphere of H_2/Ar (H_2, 10 vol %) with a total gas flow rate of 100 sccm was then used and the detained heating program is depicted in Figure S1. After cooling down to room temperature naturally, the as-produced black product was CoSe@NPC/CoSe@CNTs. Additionally, CoSe@NPC and NPC/CNTs were also produced as the control samples. CoSe@NPC was obtained by a similar process without the reducing gas H_2. Specifically, NPC/CNTs were synthesized by two steps: (i) the first step was similar to the previous procedure without Se powder. (ii) Afterward, the resultant materials were immersed into a 2 M H_2SO_4 aqueous solution with the protection of inert gas to remove exposed cobalt metal and finally NPC/CNTs were obtained after rinsing with ethanol/water and drying in a vacuum oven at 60 °C.

4.4. Fabrication of CEs for DSSCs. Briefly, after sufficient cleaning of conductive FTO glasses to remove the surface impurities, the treated FTO glasses were pretreated with 50 mM $TiCl_4$ at 70 °C for 30 min. Then, a commercial TiO_2 paste with a size of 20 nm and another TiO_2 with a size of 400 nm were cast on the FTO substrate using a doctor-blade technique. These prepared films were then heated to 450 and 500 °C for 30 min, respectively, in an air atmosphere using a muffle furnace. After cooling to room temperature, these films was immersed in 50 mM $TiCl_4$ aqueous solution for 30 min at 70 °C, followed by heating to 500 °C in an air atmosphere. After cooling to 120 °C or so, the resulting TiO_2 films were transferred into the dispersed N719 dye solution (0.5 mM) in a mixture of *tert*-butyl alcohol and acetonitrile (1:1 vol ratio) for 1 day to thoroughly adsorb and obtain dye-sensitized photoanode.

Typical sandwich-like DSSCs were assembled with an above-prepared sensitized photoanode, an acetonitrile electrolyte coupled with different CEs fabricated. A 30 μm thick Surlyn film separated the photoanode and the CE. The working electrolyte, containing 0.6 M 1-methyl-3-propylimidazoliumiodide (DMPII), 0.03 M I_2, 0.06 M LiI, and 0.5 M 4-*tert*-butyl putyl pyridine in an acetonitrile organic solvent, was injected rapidly into the gap between the two electrodes and clamped together with binder clips. As a benchmark, a Pt CE was prepared by thermally decomposing 20 μL of 20 mM H_2PtCl_6 ethanol solvent onto conductive FTO glass at 400 °C for 15 min in the air atmosphere.

4.5. Characterization. The XRD spectra of the as-made samples were collected on a Rigaku Ultima IV X-ray diffractometer with a Cu Kα radiation (λ = 1.5418 c5) operated at 40 kV and 40 mA in a scanning range of 10−90° (2θ). The morphologies of products were characterized by FESEM (Hitachi S4800) and HRTEM (JSM-2100, JEOL, Japan). XPS (PHI Quantera-II SXM) was carried out to analyze bonding configurations. N_2 adsorption−desorption isotherms were analyzed at 77 K with a Micromeritics ASAP 2020, and the analyses of surface area and pore size were fitted by BET and BJH (before this test, the samples were out-gassed

https://dx.doi.org/10.1021/acsomega.0c04022
ACS Omega 2020, 5, 26253−26261

at 200 °C for 4 h). The graphitic degree and defects were recorded by a HORIBA LabRam HR Raman spectrometer equipped with a 532 nm laser excitation. TGA was carried out by an SDT Q600-1649 instrument under the N_2 atmosphere at a ramp rate of 10 K per minuets with a temperature of 25−950 °C.

All of the electrochemical measurements were measured on an electrochemical working station (CHI 604E) and the test details could be referenced by our previous works.[48,49] It should be noted that the light intensity was calibrated using a Si solar cell (National Institute of Metrology, China).

■ ASSOCIATED CONTENT

Supporting Information

The Supporting Information is available free of charge at https://pubs.acs.org/doi/10.1021/acsomega.0c04022.

Heating program of an MSTPE; high-resolution XPS survey spectra of the C 1s CoSe@NPC/CoSe@CNT sample; XRD pattern and SEM image of the intermediate product Co@NPC/Co@CNTs; XRD pattern, SEM image, and TEM image of CoSe@NPC; and XRD pattern of selenization of ZIF-67 with different temperatures (PDF)

■ AUTHOR INFORMATION

Corresponding Authors

Hansheng Li − *School of Chemistry and Chemical Engineering, Beijing Institute of Technology, Beijing 100081, China;* orcid.org/0000-0002-6582-2270; Email: hanshengli@bit.edu.cn

Qin Wu − *School of Chemistry and Chemical Engineering, Beijing Institute of Technology, Beijing 100081, China;* Email: wuqin_bit@126.com

Authors

Tong Wang − *School of Chemistry and Chemical Engineering, Beijing Institute of Technology, Beijing 100081, China*

Yongjian Li − *School of Chemistry and Chemical Engineering, Beijing Institute of Technology, Beijing 100081, China*

Daxin Shi − *School of Chemistry and Chemical Engineering, Beijing Institute of Technology, Beijing 100081, China*

Qingze Jiao − *School of Chemistry and Chemical Engineering and School of Materials and Environment, Beijing Institute of Technology, Beijing 100081, China*

Yun Zhao − *School of Chemistry and Chemical Engineering, Beijing Institute of Technology, Beijing 100081, China;* orcid.org/0000-0002-4432-9305

Pengju Su − *School of Chemistry and Chemical Engineering, Beijing Institute of Technology, Beijing 100081, China*

Wei Wang − *School of Chemistry and Chemical Engineering, Beijing Institute of Technology, Beijing 100081, China*

Complete contact information is available at: https://pubs.acs.org/10.1021/acsomega.0c04022

Author Contributions

[§]T.W. and Y.L. contributed equally to this work.

Notes

The authors declare no competing financial interest.

■ ACKNOWLEDGMENTS

The authors sincerely acknowledged the financial support from the State Key Program of National Natural Science Foundation of China (no. 21736001) and the National Natural Science Foundation of China (no. 21576025). Furthermore, the authors thanked the technical support from the Analysis & Testing Center (Beijing Institute of Technology).

■ REFERENCES

(1) O'regan, B.; Grätzel, M. A Low-Cost, High-Efficiency Solar-Cell Based on Dye-sensitized Colloidal TiO2 Films. *Nature* **1991**, *353*, 737−740.

(2) Bi, E.; Chen, H.; Yang, X.; Peng, W.; Grätzel, M.; Han, L. A quasi core-shell nitrogen-doped graphene/cobalt sulfide conductive catalyst for highly efficient dye-sensitized solar cells. *Energy Environ. Sci.* **2014**, *7*, 2637−2641.

(3) Li, Z.; Gong, F.; Zhou, G.; Wang, Z.-S. NiS2/Reduced Graphene Oxide Nanocomposites for Efficient Dye-Sensitized Solar Cells. *J. Phys. Chem. C* **2013**, *117*, 6561−6566.

(4) Huang, K.-C.; Wang, Y.-C.; Chen, P.-Y.; Lai, Y.-H.; Huang, J.-H.; Chen, Y.-H.; Dong, R.-X.; Chu, C.-W.; Lin, J.-J.; Ho, K.-C. High performance dye-sensitized solar cells based on platinum nanoparticle/multi-wall carbon nanotube counter electrodes: The role of annealing. *J. Power Sources* **2012**, *203*, 274−281.

(5) Wang, H.; Hu, Y. H. Graphene as a counter electrode material for dye-sensitized solar cells. *Energy Environ. Sci.* **2012**, *5*, 8182−8188.

(6) Lin, K.-Y.; Nguyen, M. T.; Waki, K.; Jiang, J.-C. Boron and Nitrogen Co-doped Graphene Used As Counter Electrode for Iodine Reduction in Dye-Sensitized Solar Cells. *J. Phys. Chem. C* **2018**, *122*, 26385−26392.

(7) Moraes, R. S.; Saito, E.; Leite, D. M. G.; Massi, M.; da Silva Sobrinho, A. S. Optical, electrical and electrochemical evaluation of sputtered platinum counter electrodes for dye sensitized solar cells. *Appl. Surf. Sci.* **2016**, *364*, 229−234.

(8) Briscoe, J.; Dunn, S. The Future of Using Earth-Abundant Elements in Counter Electrodes for Dye-Sensitized Solar Cells. *Adv. Mater.* **2016**, *28*, 3802−3813.

(9) Syrrokostas, G.; Siokou, A.; Leftheriotis, G.; Yianoulis, P. Degradation mechanisms of Pt counter electrodes for dye sensitized solar cells. *Sol. Energy Mater. Sol. Cells* **2012**, *103*, 119−127.

(10) Cao, Y.; Liu, Y.; Zakeeruddin, S. M.; Hagfeldt, A.; Grätzel, M. Direct Contact of Selective Charge Extraction Layers Enables High-Efficiency Molecular Photovoltaics. *Joule* **2018**, *2*, 1108−1117.

(11) Meng, X.; Yu, C.; Song, X.; Liu, Y.; Liang, S.; Liu, Z.; Hao, C.; Qiu, J. Nitrogen-Doped Graphene Nanoribbons with Surface Enriched Active Sites and Enhanced Performance for Dye-Sensitized Solar Cells. *Adv. Energy Mater.* **2015**, *5*, 1500180.

(12) Yuan, H.; Liu, J.; Li, H.; Li, Y.; Liu, X.; Shi, D.; Wu, Q.; Jiao, Q. Graphitic carbon nitride quantum dot decorated three-dimensional graphene as an efficient metal-free electrocatalyst for triiodide reduction. *J. Mater. Chem. A* **2018**, *6*, 5603−5607.

(13) Sarkar, A.; Chakraborty, A. K.; Bera, S. NiS/rGO nanohybrid: An excellent counter electrode for dye sensitized solar cell. *Sol. Energy Mater. Sol. Cells* **2018**, *182*, 314−320.

(14) Kumar, T. R.; Akhtar, M. S.; Kumar, G. G. Ni-Co bimetallic nanoparticles anchored reduced graphene oxide as an efficient counter electrode for the application of dye sensitized solar cells. *J. Mater. Sci.: Mater. Electron.* **2017**, *28*, 823−831.

(15) Huang, S.; Wang, H.; Wang, S.; Hu, Z.; Zhou, L.; Chen, Z.; Jiang, Y.; Qian, X. Encapsulating CoS2-CoSe2 heterostructured nanocrystals in N-doped carbon nanocubes as highly efficient counter electrodes for dye-sensitized solar cells. *Dalton Trans.* **2018**, *47*, 5236−5244.

(16) Sun, C.; Guo, X.; Zhang, J.; Han, G.; Gao, D.; Gao, X. Rechargeable Zn-air batteries initiated by nickel-cobalt bimetallic selenide. *J. Energy Chem.* **2019**, *38*, 34−40.

(17) Yuan, H.; Kong, L.; Li, T.; Zhang, Q. A review of transition metal chalcogenide/graphene nanocomposites for energy storage and conversion. *Chin. Chem. Lett.* **2017**, *28*, 2180−2194.

(18) Yuan, B.; Hua, D.; Gu, X.; Shen, Y.; Xu, L.-C.; Li, X.; Zheng, B.; Wu, J.; Zhang, W.; Li, S.; Huo, F. Polar, catalytic, and conductive

CoSe2/C frameworks for performance enhanced S cathode in Li-S batteries. *J. Energy Chem.* **2020**, *48*, 128−135.
(19) Jing, H.; Song, X.; Ren, S.; Shi, Y.; An, Y.; Yang, Y.; Feng, M.; Ma, S.; Hao, C. ZIF-67 Derived Nanostructures of Co/CoO and Co@N-doped Graphitic Carbon as Counter Electrode for Highly Efficient Dye-sensitized Solar Cells. *Electrochim. Acta* **2016**, *213*, 252−259.
(20) Chen, Y.-Z.; Wang, C.; Wu, Z.-Y.; Xiong, Y.; Xu, Q.; Yu, S.-H.; Jiang, H.-L. From Bimetallic Metal-Organic Framework to Porous Carbon: High Surface Area and Multicomponent Active Dopants for Excellent Electrocatalysis. *Adv. Mater.* **2015**, *27*, 5010−5016.
(21) Zheng, Y.; Wang, X.; Zhao, W.; Cao, X.; Liu, J. Phytic acid-assisted synthesis of ultrafine NiCo2S4 nanoparticles immobilized on reduced graphene oxide as high-performance electrode for hybrid supercapacitors. *Chem. Eng. J.* **2018**, *333*, 603−612.
(22) Díaz-Duran, A. K.; Roncaroli, F. MOF derived Mesoporous Nitrogen doped Carbons with high Activity towards Oxygen Reduction. *Electrochim. Acta* **2017**, *251*, 638−650.
(23) Yuan, H.; Peng, H.-J.; Huang, J.-Q.; Zhang, Q. Sulfur Redox Reactions at Working Interfaces in Lithium-Sulfur Batteries: A Perspective. *Adv. Mater. Interfaces* **2019**, *6*, 1802046.
(24) Yuan, H.; Huang, J.-Q.; Peng, H.-J.; Titirici, M.-M.; Xiang, R.; Chen, R.; Liu, Q.; Zhang, Q. A Review of Functional Binders in Lithium-Sulfur Batteries. *Adv. Energy Mater.* **2018**, *8*, 1802107.
(25) Yuan, H.; Liu, J.; Jiao, Q.; Li, Y.; Liu, X.; Shi, D.; Wu, Q.; Zhao, Y.; Li, H. Sandwich-like octahedral cobalt disulfide/reduced graphene oxide as an efficient Pt-free electrocatalyst for high-performance dye-sensitized solar cells. *Carbon* **2017**, *119*, 225−234.
(26) Huang, S.; Li, S.; He, Q.; An, H.; Xiao, L.; Hou, L. Formation of CoTe2 embedded in nitrogen-doped carbon nanotubes-grafted polyhedrons with boosted electrocatalytic properties in dye-sensitized solar cells. *Appl. Surf. Sci.* **2019**, *476*, 769−777.
(27) Park, S.-K.; Kim, J. K.; Kang, Y. C. Excellent sodium-ion storage performances of CoSe2 nanoparticles embedded within N-doped porous graphitic carbon nanocube/carbon nanotube composite. *Chem. Eng. J.* **2017**, *328*, 546−555.
(28) Zhang, J.; Li, F.; Chen, W.; Wang, C.; Cai, D. Facile synthesis of hollow Co3O4-embedded carbon/reduced graphene oxides nanocomposites for use as efficient electrocatalysts in oxygen evolution reaction. *Electrochim. Acta* **2019**, *300*, 123−130.
(29) Zhang, Y.; Pan, A.; Ding, L.; Zhou, Z.; Wang, Y.; Niu, S.; Liang, S.; Cao, G. Nitrogen-Doped Yolk-Shell-Structured CoSe/C Dodecahedra for High-Performance Sodium Ion Batteries. *ACS Appl. Mater. Interfaces* **2017**, *9*, 3624−3633.
(30) Li, J.; Yan, D.; Lu, T.; Yao, Y.; Pan, L. An advanced CoSe embedded within porous carbon polyhedra hybrid for high performance lithium-ion and sodium-ion batteries. *Chem. Eng. J.* **2017**, *325*, 14−24.
(31) Chen, M.; Zhao, G.; Shao, L.-L.; Yuan, Z.-Y.; Jing, Q.-S.; Huang, K.-J.; Huang, Z.-Y.; Zhao, X.-H.; Zou, G.-D. Controlled Synthesis of Nickel Encapsulated into Nitrogen-Doped Carbon Nanotubes with Covalent Bonded Interfaces: The Structural and Electronic Modulation Strategy for an Efficient Electrocatalyst in Dye-Sensitized Solar Cells. *Chem. Mater.* **2017**, *29*, 9680−9694.
(32) Meng, J.; Niu, C.; Xu, L.; Li, J.; Liu, X.; Wang, X.; Wu, Y.; Xu, X.; Chen, W.; Li, Q.; Zhu, Z.; Zhao, D.; Mai, L. General Oriented Formation of Carbon Nanotubes from Metal-Organic Frameworks. *J. Am. Chem. Soc.* **2017**, *139*, 8212−8221.
(33) Ali, Z.; Tang, T.; Huang, X.; Wang, Y.; Asif, M.; Hou, Y. Cobalt selenide decorated carbon spheres for excellent cycling performance of sodium ion batteries. *Energy Storage Mater.* **2018**, *13*, 19−28.
(34) Tang, Y.; Zhao, Z.; Hao, X.; Wang, Y.; Liu, Y.; Hou, Y.; Yang, Q.; Wang, X.; Qiu, J. Engineering hollow polyhedrons structured from carbon-coated CoSe2 nanospheres bridged by CNTs with boosted sodium storage performance. *J. Mater. Chem. A* **2017**, *5*, 13591−13600.
(35) Xia, B. Y.; Yan, Y.; Li, N.; Wu, H. B.; Lou, X. W.; Wang, X. A metal−organic framework-derived bifunctional oxygen electrocatalyst. *Nat. Energy* **2016**, *1*, 15006.
(36) Lu, H.-S.; Zhang, H.; Liu, R.; Zhang, X.; Zhao, H.; Wang, G. Macroscale cobalt-MOFs derived metallic Co nanoparticles embedded in N-doped porous carbon layers as efficient oxygen electrocatalysts. *Appl. Surf. Sci.* **2017**, *392*, 402−409.
(37) Hu, H.; Zhang, J.; Guan, B.; Lou, X. W. D. Unusual Formation of CoSe@carbon Nanoboxes, which have an Inhomogeneous Shell, for Efficient Lithium Storage. *Angew. Chem., Int. Ed.* **2016**, *55*, 9514−9518.
(38) Liao, M.; Zeng, G.; Luo, T.; Jin, Z.; Wang, Y.; Kou, X.; Xiao, D. Three-dimensional coral-like cobalt selenide as an advanced electrocatalyst for highly efficient oxygen evolution reaction. *Electrochim. Acta* **2016**, *194*, 59−66.
(39) Lin, C.; Shinde, S. S.; Jiang, Z.; Song, X.; Sun, Y.; Guo, L.; Zhang, H.; Jung, J.-Y.; Li, X.; Lee, J.-H. In situ directional formation of Co@CoOx-embedded 1D carbon nanotubes as an efficient oxygen electrocatalyst for ultra-high rate Zn-air batteries. *J. Mater. Chem. A* **2017**, *5*, 13994−14002.
(40) Hou, S.; Cai, X.; Wu, H.; Yu, X.; Peng, M.; Yan, K.; Zou, D. Nitrogen-doped graphene for dye-sensitized solar cells and the role of nitrogen states in triiodide reduction. *Energy Environ. Sci.* **2013**, *6*, 3356.
(41) Liu, M.; Lin, H.; Mei, Z.; Yang, J.; Lin, J.; Liu, Y.; Pan, F. Tuning Cobalt and Nitrogen Co-Doped Carbon to Maximize Catalytic Sites on a Superabsorbent Resin for Efficient Oxygen Reduction. *ChemSusChem* **2018**, *11*, 3631−3639.
(42) Park, S.-H.; Kim, B.-K.; Lee, W.-J. Electrospun activated carbon nanofibers with hollow core/highly mesoporous shell structure as counter electrodes for dye-sensitized solar cells. *J. Power Sources* **2013**, *239*, 122−127.
(43) Yuan, H.; Peng, H.-J.; Li, B.-Q.; Xie, J.; Kong, L.; Zhao, M.; Chen, X.; Huang, J.-Q.; Zhang, Q. Conductive and Catalytic Triple-Phase Interfaces Enabling Uniform Nucleation in High-Rate Lithium-Sulfur Batteries. *Adv. Energy Mater.* **2018**, *9*, 1802768.
(44) Chen, T.; Li, S.; Wen, J.; Gui, P.; Guo, Y.; Guan, C.; Liu, J.; Fang, G. Rational Construction of Hollow Core-Branch CoSe2 Nanoarrays for High-Performance Asymmetric Supercapacitor and Efficient Oxygen Evolution. *Small* **2018**, *14*, 1700979.
(45) Li, Z.; Shao, M.; Zhou, L.; Zhang, R.; Zhang, C.; Wei, M.; Evans, D. G.; Duan, X. Directed Growth of Metal-Organic Frameworks and Their Derived Carbon-Based Network for Efficient Electrocatalytic Oxygen Reduction. *Adv. Mater.* **2016**, *28*, 2337−2344.
(46) Younas, M.; Gondal, M. A.; Dastageer, M. A.; Baig, U. Fabrication of cost effective and efficient dye sensitized solar cells with WO3-TiO2 nanocomposites as photoanode and MWCNT as Pt-free counter electrode. *Ceram. Int.* **2019**, *45*, 936−947.
(47) Xia, W.; Zhu, J.; Guo, W.; An, L.; Xia, D.; Zou, R. Well-defined carbon polyhedrons prepared from nano metal-organic frameworks for oxygen reduction. *J. Mater. Chem. A* **2014**, *2*, 11606−11613.
(48) Yuan, H.; Jiao, Q.; Liu, J.; Liu, X.; Li, Y.; Shi, D.; Wu, Q.; Zhao, Y.; Li, H. Facile synthesis of Co0.85Se nanotubes/reduced graphene oxide nanocomposite as Pt-free counter electrode with enhanced electrocatalytic performance in dye-sensitized solar cells. *Carbon* **2017**, *122*, 381−388.
(49) Yuan, H.; Liu, J.; Li, H.; Su, K.; Liu, X.; Li, Y.; Shi, D.; Wu, Q.; Zhao, Y.; Jiao, Q. Rational integration of hierarchical structural CoS1.097 nanosheets/reduced graphene oxide nanocomposites with enhanced electrocatalytic performance for triiodide reduction. *Carbon* **2018**, *126*, 514−521.

https://dx.doi.org/10.1021/acsomega.0c04022
ACS Omega 2020, 5, 26253−26261